Strongly coupled piezoelectric energy harvesters: finite element modelling and experimental validation

Yang Kuang, Zheng Jun Chew, Meiling Zhu*

*Corresponding author: m.zhu@exeter.ac.uk

College of Engineering, Mathematics and Physical Sciences, University of Exeter, Exeter, EX4 4QF, UK

Abstract

Piezoelectric energy harvesters (PEHs) are usually connected to a load resistor R_L matching to the impedance of their internal capacitance C_P^T to characterise the power generation during transducer design and optimisation. For strongly-coupled PEHs operating near resonance, this simple RC matching method underestimates the power output and fails to characterise the dual power peaks but are still often used in both simulation and experiment. This study analysed the internal impedance network and the power output characteristics of PEHs. Based on the analysis, a novel and efficient finite element model (FEM) for strongly coupled PEHs was developed and applied to a pre-stressed piezoelectric stack energy harvester (PSEH). A stationary analysis was first performed to simulate the pre-stressed state of the PSEH. The FEM then analysed the internal impedance of the pre-stressed PSEH, which was used as the optimal load resistance to simulate the electric power output. The simulated internal impedance and electric power output of the PSEH were validated by the experiment with good agreement. The FEM developed precisely predicted the electric power output, including the two identical power peaks, of the strongly coupled PSEH operating near resonance and outside resonance. In contrast, the FEM with the traditional RC matching showed only one power peak and significantly underestimated the power output near resonance, although it was still valid outside resonance. The developed FEM was also able to predict the effects of the static pre-stress and coupling efficiency figure of merit on the PSEH. The coupling efficiency figure of merit was found to increase the power output.

Keywords: piezoelectric energy harvesting; electric impedance; finite element modelling; pre-stressed; strongly coupled

Nomenclature		Z_{in}	Internal impedance of a PEH (Ω)
PEH	Piezoelectric energy harvester	$\lvert Z_{in} \rvert$	Magnitude of internal impedance (Ω)
PSEH	Piezoelectric stack energy harvester	Y_{in}	Internal admittance of a PEH (S)
FEM	Finite element model	G	Conductance, the real part of Y_{in} (S)
SDOF	Single degree of freedom	B	Susceptance, the imaginary part Y_{in} (S)
ECM	Equivalent circuit model	G_{max}	The maximum conductance value (S)
K	Electromechanical coupling coefficient	ω_s	Short circuit resonance frequency (rad/s)
Q_M	Mechanical quality factor	$B(\omega_s)$	Conductance value at ω_s (S)
$K^2 Q_M$	Coupling efficiency figure of merit	ω_1, ω_2	Frequencies at which the conductance value is $\frac{1}{2R_m}$ (rad/s)
m	Proof mass of a PEH (kg)	ω_{01}, ω_{02}	Angular frequencies with zero impedance phase and $\omega_{01} < \omega_{02}$ (rad/s)
c_d	Damping coefficient of a PEH	f_{01}, f_{02}	Frequencies with zero impedance phase and $f_{01} < f_{02}$ (Hz)
k	Stiffness of a PEH (N/m)	f_m	The frequency with the maximum impedance phase (Hz)
x	Displacement of a PEH (m)	β	Tilted angle of the inclined beams in the mechanical transformer (°)
C_P^S	Clamped capacitance of a PEH (F)	F_x	Input force to the PSEH along the x-axis (N)
C_P^T	Free capacitance of a PEH (F)	D_x	Input displacement to the PSEH along the x-axis (m)
Λ	Force factor of a PEH (N/V)	F_z	Force applied to the piezoelectric element (N)

V_P	Output voltage on a load resistance (V)	D_z	Displacement of the piezoelectric element (m)
I_P	Output current through a load resistance (A)	k_x	Stiffness of the PSEH in the x-axis (N/m)
R_L	Load resistance (Ω)	k_z	Stiffness of the PSEH in the z-axis (N/m)
R_{opt}	The optimal load resistance (Ω)	L_z	Length of the PSEH along the z-axis (mm)
A_0	Amplitude of the harmonic acceleration (m/s^2)	ΔL_z	Change of L_z due to the pre-force (μm)
ω	Angular frequency (rad/s)	L_x	Length of the PSEH along the x-axis (mm)
C_m	Capacitance in the equivalent circuit model (F)	ΔL_x	Change of L_x due to the pre-force (μm)
R_m	Resistance in the equivalent circuit model (Ω)	N	Number of active piezoelectric layers in the multilayer piezoelectric stack
L_m	Inductance in the equivalent circuit model (H)	s_{ij}^E	Elastic compliance tensor at the constant condition (m^2/N)
V_{eq}	Voltage in the equivalent circuit model (V)	$\smile$	Variables corresponding to the single-layer piezoelectric element used in the FEM
F_s	The static force applied to the mechanical transformer without the piezoelectric element in the FEM, i.e. estimated static force applied to the fabricated PSEH (N)	F_0	The static force applied to the PSEH in the FEM for impedance and power simulation

1. Introduction

Piezoelectric energy harvesting has been intensively investigated in the past two decades, aiming to provide a sustainable power source for wireless electronics by converting the ambient vibrations to usable electricity [1]. It is well known that the power output of a piezoelectric energy harvester (PEH) is highly dependent on the impedance of the load. Although complicated power management circuits are required to transfer the power efficiently from the PEHs to energy storages [2], a load resistor is usually connected to characterise the generated power during the transducer design and optimisation stage. The optimal load resistance is the one yielding the maximum power consumption on the load resistor. In the simplest form, a piezoelectric energy harvester can be considered as two decoupled mechanical and electrical systems. It is usually modelled as an equivalent circuit model with a current source connected in parallel or a voltage source connected in series to the free capacitor of the piezoelectric material [3, 4]. The optimal resistance is therefore considered as the impedance of the free capacitor (referred to as RC matching) [5]. The RC matching method has satisfactory accuracy for all PEHs operating outside the resonance [6] and for weakly coupled PEHs operating near resonance [7], due to the capacitive nature of PEHs in these cases and thereby has been widely used in both modelling and experiment. However, for strongly coupled PEHs operating near resonance, the RC matching method was found to be inaccurate [8]. For instance, the power output of strongly coupled PEHs has two identical peaks near resonance [9], which cannot be observed with the RC matching method in either experiment or simulation.

To predict the electric power output of PEHs more accurately, analytical models have been developed to derive the full expression of power output, which is then analysed to identify the optimal load resistance and peak power [10]. Through analytical models, Renno *et al.* [11] and Goldschmidtboeing *et al.* [12] found that two power peaks and two optimal load resistance values may exist near the resonance of a PEH when the electromechanical coupling coefficient K is high enough or the mechanical damping is low enough. This phenomenon was also observed by Liao and Sodano [13] in both experiment and analytical modelling. They found that if the RC matching method was used, only a single power peak could be observed, which confirmed the inaccuracy of the RC matching method for strongly coupled PEHs near resonance. Analytical models can precisely predict optimal resistance and maximum power generation. They can be quite useful for design optimisation of PEHs. However, they do not provide a physical and intuitive explanation for the power characteristics of strongly-coupled PEHs. Moreover, the closed form expression of the power output may not be available when the structure of the PEH becomes complicated or nonlinear [14, 15].

55   Equivalent circuit models (ECMs) of PEHs based on lumped parameters have been developed and implemented
56   in simulation tools such as SPICE. The lumped parameters can be determined by either analytical modelling [16]
57   or finite element analysis [17]. Kong *et al.* [18] derived the internal impedance network of PEHs based on the
58   analogy between electrical and mechanical domains. The internal impedance network was found far more
59   complicated than the free capacitor as used in the RC matching method. They pointed out that with a resistive
60   impedance matching, the maximum power transfer was available at frequencies with a purely resistive internal
61   impedance, i.e. the impedance phase is zero. When the zero-phase is not available, the load resistance should still
62   match the internal impedance magnitude to achieve a sub-optimal matching [18]. This was further investigated
63   by Lei *et al.* [19], who showed that when the coupling efficiency figure of merit $K^2 Q_M$ (Q_M being the mechanical
64   quality factor) was larger than 2, the internal impedance of the PEH had two zero-phase frequencies near
65   resonance and therefore two power peaks were available. The link of power peaks to the zero-impedance-phase
66   provides a sensible explanation to the double power peaks of strongly coupled PEHs. ECMs with lumped
67   parameters are useful for designing the power management circuits [20, 21] after the design of a PEH is finished
68   and thus the lumped parameters are fixed. However, it is not convenient for the design and optimisation of energy
69   harvesters because the design parameters such as geometry and material properties are not directly reflected in
70   the lumped parameters [22].

71   For energy harvester design and optimisation, commercial software packages such as ANSYS and COMSOL
72   provides a powerful tool because of their ability to simulate complicated transducer structures [23, 24] and more
73   importantly to couple the fields of mechanical structures, piezoelectricity and electrical circuits. This enables the
74   development of piezoelectric-circuit coupled finite element models (FEMs), in which piezoelectric energy
75   harvesters are connected to electrical circuits. This provides a direct link between physical design parameters and
76   the electric power output. The first coupled piezoelectric-circuit coupled FEM was developed by Zhu *et al.* [25]
77   in ANAYS to analyse the power output of piezoelectric cantilever connected to a load resistor, but it is for weakly
78   coupled piezoelectric energy harvesters although there is no mention on this. Since then, similar FEMs have been
79   developed to simulate the performance of various PEHs [26-28]. Cheng *et al.* [22] modelled the nonlinear
80   synchronized switch harvesting on inductor as an equivalent linear electric impedance in COMSOL thus enabling
81   the finite element modelling of PEH connected to a nonlinear circuit. For strong coupled piezoelectric energy
82   harvester, although the internal impedance network of a PEH is far more complicated than the free capacitor of
83   the piezoelectric material, most FEMs still use the simple RC matching method, i.e. using a load resistance to
84   match the impedance of the capacitor, which could lead to inaccurate results for strongly coupled PEHs operating
85   near resonance. FEMs for strongly coupled PEHs have not been reported so far. This work proposes a novel and
86   efficient finite element modelling method for strongly-coupled PEHs connected to a load circuit. The FEM first
87   analyses the internal impedance of the PEH across the frequency range of interest. The impedance magnitudes are
88   then used as the value of the optimal load resistance at the corresponding frequency to simulate the power
89   generation. Using the proposed method, the full performance of the PEH including the optimal load resistance
90   and the maximum power output across the whole frequency range can be accurately simulated, regardless of the
91   degree of electromechanical coupling. The method can be applied to any harmonically actuated linear PEHs or
92   nonlinear PEHs that can be linearized around the operating point.

93   2. Optimal load resistance and power out characteristics of PEHs

94   In this section, the theories behind the optimal load resistance and power output characteristics of PEHs are
95   revisited to provide guidance for the finite element modelling.

96   2.1 Internal impedance of PEHs

97   The majority of piezoelectric energy harvesters can be regarded as an oscillator with single-degree-of-freedom
98   (SDOF) and working at the fundamental mode. Considering a single SDOF PEH subjected to harmonic excitation
99   at its base, its dynamic behaviours can be described by (1) [21].

$$m\ddot{x}(t) + c_d \dot{x}(t) + kx(t) + \Lambda V_p(t) = mA_0 cos(\omega t)$$

$$I_P(t) + C_P^S \dot{V}_P(t) = \Lambda \dot{x}(t) \qquad\qquad (1)$$

100 where m is the mass, c_d the mechanical damping coefficient, k the stiffness, x the displacement, C_P^S the clamped
101 capacitance, Λ the force factor, V_P the output voltage, I_P the output current, A_0 the amplitude and ω the
102 frequency of excitation acceleration, respectively.

103 According to the analogy between mechanical and electrical systems, the system described by (1) can be
104 represented by an equivalent circuit model as shown in Figure 1 (a). The inertial mass m, compliance $1/k$ and
105 mechanical damping c_d are represented by the inductor, capacitor, and resistor respectively. The
106 electromechanical coupling of the piezoelectric element is represented as an ideal transformer with a
107 transformation factor of $\Lambda\!:\!1$. The excitation force is modelled as a harmonic voltage source with an amplitude of
108 mA. The model in (a) can be simplified to (b) by taking the equivalence in (2).

$$C_m = \frac{\Lambda^2}{k} \qquad R_m = \frac{c_d}{\Lambda^2}$$

$$L_m = \frac{m}{\Lambda^2} \qquad V_{eq} = \frac{mA}{\Lambda} \qquad (2)$$

109 where C_m, R_m, L_m and V_{eq} are the capacitance, resistance, inductance and equivalent voltage, respectively.
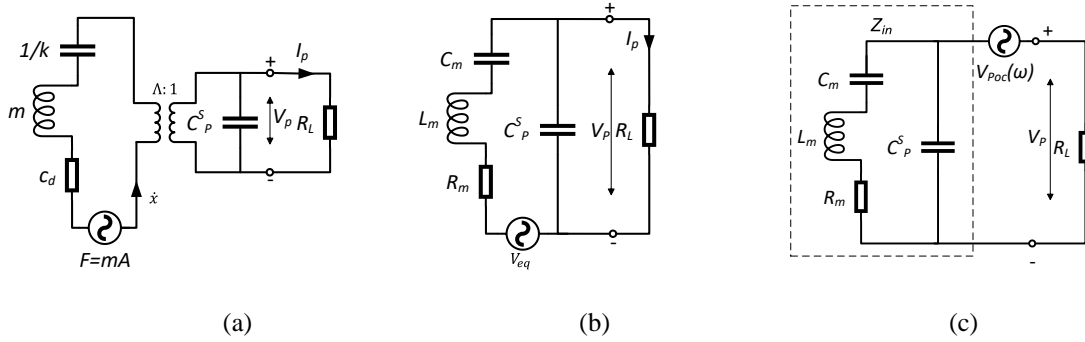
111   (a)   (b)   (c)
112 Figure 1 Equivalent circuit models of single-degree-of-freedom piezoelectric energy harvesters operating near
113 the fundamental resonance: (a) original equivalent circuit model; (b) simplified model by taking the transformer
114 equivalence; (c) resultant model by applying Thevenin's Theorem on (b)

115 The ECM in Figure (b) can be further transformed to Figure (c) by applying Thevenin's Theorem. In Figure (c),
116 the PEH is modelled as an AC voltage source with an internal impedance Z_{in} connected in series to R_L. The
117 amplitude of the voltage source is the output voltage V_P measured at open-circuited condition, denoted as $V_{Poc}(\omega)$
118 and is frequency-dependent. The internal impedance network consists of a motional branch (C_m, L_m and R_m) and
119 the clamped capacitor C_P^S connected in parallel. It is clearly far more complicated than just a capacitor, which is
120 assumed when using the RC matching method.

121 The values of the components in the ECMs can be identified from the measured or simulated internal impedance
122 characteristics by using (3) [29].

$$R_m = \frac{1}{G_{max}} \qquad C_P^S = \frac{B(\omega_s)}{\omega_s}$$

$$C_m = \frac{\omega_2 - \omega_1}{R_m \omega_1 \omega_2} \qquad L_m = \frac{1}{\omega_s^2 C_m} = \frac{R_m}{\omega_2 - \omega_1} \qquad (3)$$

123 where ω_s is the short-circuit resonance frequency that has the maximum conductance value G_{max}; $B(\omega_s)$ the
124 susceptance value at ω_s; ω_1 and ω_2 are the two frequencies with a conductance value of $1/(2R_m)$. The voltage
125 V_{eq} can be calculated as

$$V_{eq} = I_{sc}(\omega_s)R_m \qquad (4)$$

126 where $I_{sc}(\omega_s)$ is the short-circuited current generated at ω_s.

127   2.2 Power output characteristics of PEHs with resistive impedance matching

128   At each frequency, the PEH is a voltage source V_{Poc} with a complex internal impedance Z_{in}. According to the
129   maximum power transfer theorem, the maximum power delivery occurs only when the load is a complex conjugate
130   matching of Z_{in}. The maximum power that can be delivered is [18]

$$P_{max} = \frac{V_{eq}^2}{8R_m} \tag{5}$$

131   However, a complex conjugate matching across the whole resonance range is difficult because of the large and
132   varied inductance required at different frequencies [18]. Instead, a load resistor is usually used to match the
133   internal impedance in the energy harvester design stage. With a resistive load, the conjugate impedance matching
134   occurs when the phase of the internal impedance is zero, i.e. the internal impedance is purely resistive. In such a
135   case, the maximum power transfer occurs and P_{max} is delivered to the load resistance. At frequencies with non-
136   zero-phase, conjugate impedance matching is not possible with a resistive load and therefore the maximum power
137   transfer cannot be achieved. However, the load resistance should still be selected to match $|Z_{in}|$ to obtain the sub-
138   maximum power although this power will be lower than P_{max}. Therefore, with a resistive load, power peaks of a
139   PEH are located at zero-phase frequencies if available and the number of power peaks depends on the number of
140   zero-phase frequency.

141   When the impedance phase of the PEH is always negative, a conjugate impedance matching is not possible with
142   the resistive load across the whole resonance region. In this case, a single power peak occurs at the frequency with
143   the maximum internal impedance-phase because at this frequency, the internal impedance has the minimum
144   reactive component, i.e. it is mostly close to being purely resistive, which has been mathematically proved in [19].

145   At low frequencies where the PEH can be regarded as quasi-static, the contribution of L_m and R_m to Z_{in} is
146   negligible compared to C_m. As a result, the internal impedance network can be approximated by C_m and C_P^S
147   connected in parallel, which equals to the free capacitor C_P^T of the PEH [17]. This leads to the traditional RC
148   matching method with the optimal load resistance R_{opt} being

$$R_{opt} = \frac{1}{\omega C_P^T} \tag{6}$$

149   2.3 Conditions for the existence of zero-phase frequencies

150   Since the zero-phase frequency plays an important role in the power output characteristics of PEHs, the conditions
151   for its existence are derived in this section by using a more intuitive method—graphic analysis than the traditional
152   analytical modelling [19]. Instead of using the internal impedance directly, the admittance of the internal
153   impedance network was used because the unique characteristics of conductance and susceptance can simplify the
154   analysis. It is noted that the phase of the admittance is opposite to that of the impedance.

155   The complex admittance Y_{in} of the internal impedance network shown in Figure 1 (c) is [30]

$$Y_{in} = \frac{1}{Z_{in}} = \frac{R_m}{R_m^2 + \left(\omega L_m - \frac{1}{\omega C_m}\right)^2} + j\left[\omega C_P^S - \frac{\omega L_m - \frac{1}{\omega C_m}}{R_m^2 + \left(\omega L_m - \frac{1}{\omega C_m}\right)^2}\right] \tag{7}$$

156   The real and imaginary parts of the Y_{in} are the conductance G and susceptance B, respectively. The relationship
157   between G and B near resonance can be re-written as

$$\left(G - \frac{1}{2R_m}\right)^2 + (B - \omega_s C_P^S)^2 = \left(\frac{1}{2R_m}\right)^2 \tag{8}$$

158   The typical locus of G-B for a PEH is presented in Figure 2 (a). It is a circle with a diameter of $1/R_m$ and its
159   centre O_1 at $(1/(2R_m), \omega_s C_P^S)$. The two intersections of the G-B locus with $B=0$ (G-axis), denoted as ω_{01} and ω_{02},
160   are corresponding to the zero-phase frequencies, at which a complex conjugate impedance matching by a load

161 resistance is available. Therefore, a PEH with a G-B circle as Figure 2 (a) has two power peaks across near
162 resonance. Obviously, ω_{01} and ω_{02} are always available as long as $\omega_s C_P^S < 1/(2R_m)$. Considering the
163 mechanical quality factor Q_M and the electromagnetic coupling factor K in (9) [8, 17], the condition for the
164 existence of ω_{01} and ω_{02} can be rewritten by (10), which agrees with the expression derived by using maa
165 thematical method in [19].

166
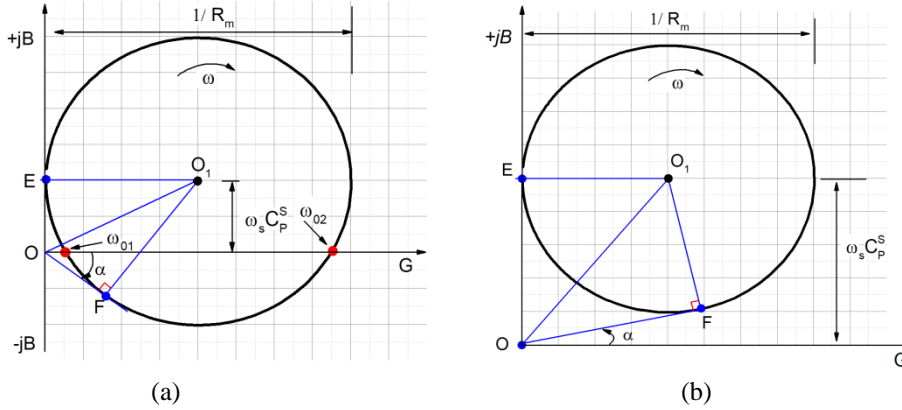
167   (a)   (b)
168 Figure 2 Locus diagram of the internal admittance of a piezoelectric energy harvester near resonance when: (a)
169 $\omega_s C_P^S < 1/(2R_m)$, i.e. $K^2 Q_M > 2$ and (b) $\omega_s C_P^S > 1/(2R_m)$, i.e. $K^2 Q_M < 2$. G-axis is located at $B=0$

$$Q_M = \frac{\omega_s}{\omega_2 - \omega_1} = \frac{1}{\omega_s R_m C_m} \qquad\qquad K^2 = \frac{\Lambda^2}{k C_P^S} = \frac{C_m}{C_P^S} \qquad\qquad (9)$$

$$K^2 Q_M > 2 \qquad\qquad (10)$$

170 When $\omega_s C_P^S > 1/(2R_m)$ or $K^2 Q_M < 2$, the G-B circle has no intersection with the B=0, i.e. no zero-phase
171 frequency as shown in Figure 2 (b). Compared to figure (a), the centre of the G-B circle in (b) was moved-up
172 while the diameter was kept unchanged, simulating the case when C_P^S is increased (K is reduced according to (9)).
173 The loss of zero-phase can also be caused by the shrink in the diameter of the G-B circle due to increased
174 mechanical damping R_m, which will be demonstrated in Section 5.4. Without the zero-phase frequency, the power
175 peak is available at the maximum-impedance-phase frequency (the minimum-admittance-phase frequency),
176 although conjugate impedance matching is not possible with a resistive load. When $\omega_s C_P^S = 1/(2R_m)$ or
177 $K^2 Q_M = 2$, the G-B locus will have one intersection with $B = 0$ and a single power peak is available at the single
178 zero-phase frequency.

179 It is noted that the internal admittance magnitude of the PEH at the minimum-admittance-phase frequency is
180 always $\omega_s C_P^S$ regardless of $K^2 Q_M$. The minimum admittance-phase frequencies correspond to point F in Figure 2,
181 where the line $\overline{OF}$ is tangent to G-B locus. The angle α between $\overline{OF}$ and G-axis is the minimum admittance phase
182 in each case. Because triangles OO_1E and OO_1F are congruent, $|\overline{OF}|$ always equals to $|\overline{OE}|$ and $\omega_s C_P^S$. In other
183 words, the internal impedance magnitude and the optimal load resistance of a PEH at the maximum-impedance-
184 phase frequency is always $1/(\omega_s C_P^S)$.

185 In light of the importance of $K^2 Q_M$ on the power output characteristics of PEH, $K^2 Q_M$ is usually referred to as the
186 coupling efficiency figure of merit [19]. PEHs with $K^2 Q_M > 2$ are strongly-coupled, have two zero-phase
187 frequencies and two power peaks near resonance; PEHs with $K^2 Q_M \leq 2$ are weakly-coupled, have a single or no
188 zero-phase frequency and a single power peak near resonance.

189 **3. Piezoelectric stack energy harvester**

190 A piezoelectric stack energy harvester (PSEH) with a mechanical transformer was used to study in this work,
191 which is a good example of strongly coupled PEH. Similar harvesters have been widely studied for low-frequency
192 compressive force energy harvesting [31-34] due to the high electrical power output, which is a result of the force
193 amplification mechanism and the high electromechanical coupling of piezoelectric stacks used [35].

194   3.1 Working mechanism

195   A schematic of the PSEH with a mechanical transformer is shown in Figure 3. It consists of a mechanical
196   transformer and a piezoelectric element usually in the form of a multilayer piezoelectric stack. The inclined beams
197   of the mechanical transformer have a tilted angle β. Both ends of each inclined beam serve as flexure hinges. To
198   simplify the analysis, it is assumed that the hinges are free to flexure while the inclined beams do not change its
199   length. In a quasi-static state, the following relationship can be obtained [33, 36]

$$F_z = F_x \cot \beta \quad\quad D_x = D_z \cot \beta$$

(11)

200   where F_x and D_x are the input force and displacement; F_z and D_z are the force and displacement of the
201   piezoelectric element.
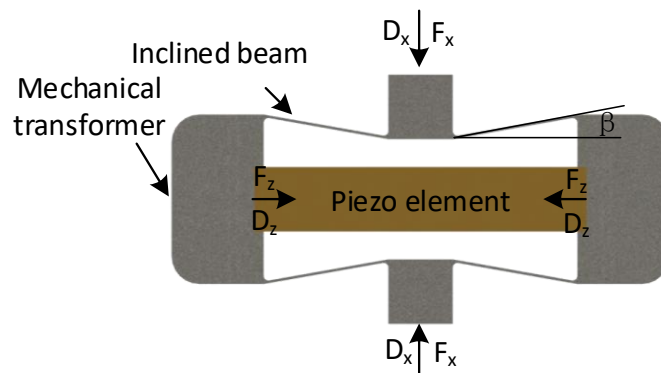
202

203   Figure 3 The operation principle of the PSEH with a mechanical transformer

204   Eq. (11) suggests that when β is small, the mechanical transformer amplifies the input force F_x by a factor of
205     $\cot \beta$ to the force F_z applied on the piezoelectric element. It is this force amplification mechanism that attracts the
206   wide interests from energy harvesting research community because the electric power output of a PEH increases
207   proportionally with the square of the force applied on the piezoelectric material. Eq. (11) also indicates that while
208   amplifying the force, the mechanical transformer reduces the displacement D_x by a factor of $\cot \beta$. This leads to
209   the stiffness along x-axis (k_x) to be lower than that along z-axis (k_z) since

$$k_x = \frac{F_x}{D_x} = \frac{1}{\cot^2 \beta} \cdot \frac{F_z}{D_z} = \frac{k_z}{\cot^2 \beta}$$

(12)

210   Piezoelectric elements have high stiffness, leading to a resonance frequency usually in the range of tens of
211   kilohertz, in contrast to the usual low frequencies (from a few to hundreds of hertz) of ambient vibrations. The
212   reduction in the stiffness can lower the resonance frequency of the PSEH to match the ambient vibration. Although
213   Eqs. (11-12) can be used for qualitative analysis, it must be noted that in reality, the relationship between the
214   force/displacement amplification and the tilted angle is more complicated due to the elastic deformation of the
215   inclined beams [33, 34, 36].

216   3.2 Design, fabrication and testing method

217   The PSEH designed for this study is shown in Figure 4 (a). Given that the focus of this study is the modelling of
218   the PSEH, the design optimisation of the mechanical transformer is not presented herein. Notably, a notch hinge
219   design was used for the inclined beams where the thickness of the flexure hinges was much smaller than the
220   middle section of the inclined beam. This is to allow easy bending of the hinges while reducing the elastic
221   deformation and energy storage in the inclined beams [36].

222   A multilayer piezoelectric stack (7×7×36 mm, PI ceramic) was used for the PSEH. The piezoelectric stack is made
223   of ~560 layers of active piezoelectric material working at 33-mode (PIC252, layer thickness: ~60 µm including

224 electrodes) and 2 passive piezoelectric layers (~0.5 mm thick), one on each end. The active piezoelectric layers
225 are electrically connected in parallel. The mechanical transformer was made of spring steel and fabricated by
226 electrical discharge machining. The space on the mechanical transformer was machined to be ~50 µm shorter
227 than the multilayer piezoelectric stack as shown in Figure 4 (b). During assembling, the mechanical transformer
228 was stretched along the z-axis so that the piezoelectric stack could slide into space. Upon release, the mechanical
229 transformer was subjected to deformation, leading to an increase in both L_x (denoted as ΔL_x) and L_z (denoted as
230 ΔL_z). As a result, the mechanical transformer applied a static compressive force to the piezoelectric stack, which
231 is essential for reliable operation since piezoelectric material has low tensile strength and high compressive
232 strength. Adhesive epoxy was used on the interfacing surfaces between the piezoelectric stack and the mechanical
233 transformer to further secure the connection. After assembling, ΔL_z and ΔL_x was measured by a micrometer
234 (resolution of 10 µm) as 69 and 660 µm, respectively.

235
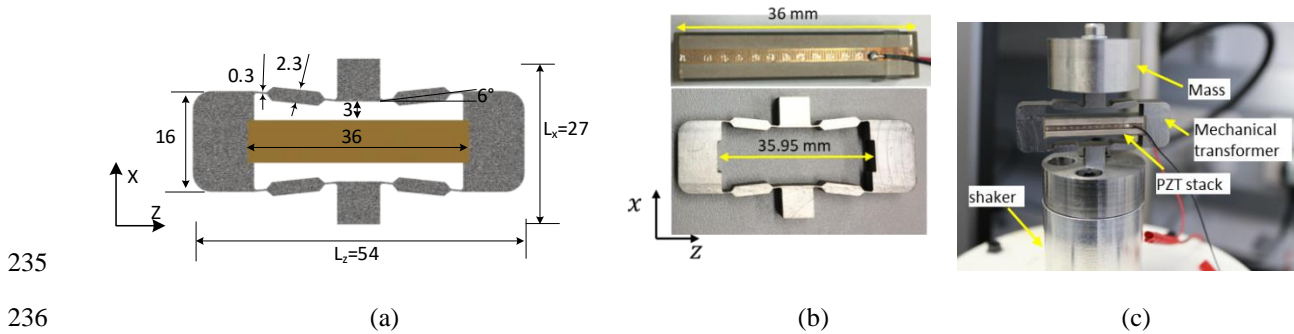
236   (a)   (b)   (c)
237   Figure 4 (a) Designed PSEH with a mechanical transformer: unit in mm unless specified, (b) the fabricated
238   mechanical transformer and multilayer piezoelectric stack used for the PEH, and (c) fully assembled PSEH
239   installed on a shaker for testing

240 The fabricated PSEH is shown in Figure 4 (c). A 100-gram mass was added on the PSEH to produce inertial force
241 and reduce the resonance frequency. The internal impedance of the PSEH was measured by a frequency response
242 analyser (PSM1700, Newton 4th). The internal impedance was converted to admittance to calculate the mechanical
243 quality factor Q_M by using (9). To measure the electric power generation, the PSEH was installed on an
244 electromagnetic shaker (V20, Data Physics). The harmonic acceleration produced by the shaker was measured by
245 a laser Doppler vibrometer (CLV 2534, Polytech). The PSEH was connected to a variable load resistor, the voltage
246 across which was recorded to calculate the power output. For each excitation frequency, the load resistor was
247 varied until the maximum power and the optimal load resistance were found.

4. Finite element modelling methods

249 Finite element modelling was used to aid the design of the PSEHs [31, 34, 36]. However, these FEMs were only
250 able to simulate the mechanical responses, not the electrical output, which severely limits their usefulness.
251 Moreover, the PSEHs are usually strongly coupled but the RC matching method was used in modelling and may
252 lead to inaccurate results. Furthermore, static compressive stress on the piezoelectric stacks is essential to
253 compensate for their weakness to tensile stress. The static prestress may affect the performance of the PSEH but
254 the effects have not been modelled.

255 A finite element model of the PSEH described in Section 3.2 was therefore developed in COMSOL Multiphysics
256 ® (COMSOL Inc, UK), which is able to accurately predict the power output of the pre-stressed and strongly
257 coupled energy harvester. Because the analysis in Section 2 suggests that the optimal load resistance is the internal
258 impedance magnitude, the internal impedance is first simulated in the developed FEM and is then used as the load
259 resistance for power generation simulation. The method described in this section can be used for any harmonically
260 excited linear PEHs or nonlinear PEHs that can be linearized around the operating point. The PEHs can be
261 connected to a linear interfacing circuit that does not contain nonlinear components such as diodes and transistors.

262   4.1 General considerations

263   The 3D physical model is comprised of the mechanical transformer and the piezoelectric element, which is shown
264   in Figure 5 in 2D for better presentation. The dimensions are shown in Figure 4 (a). A 100-gram mass was added
265   to the top surface of the mechanical transformer by applying COMSOL boundary condition without building a
266   physical mass. The dimension of the piezoelectric element was 7×7×36 mm, which was all treated as active
267   material in the model since the volume fraction of the passive layer was only 2.7% of the multilayer piezoelectric
268   stack. The mechanical damping of the PSEH was specified as a mechanical quality factor Q_M.
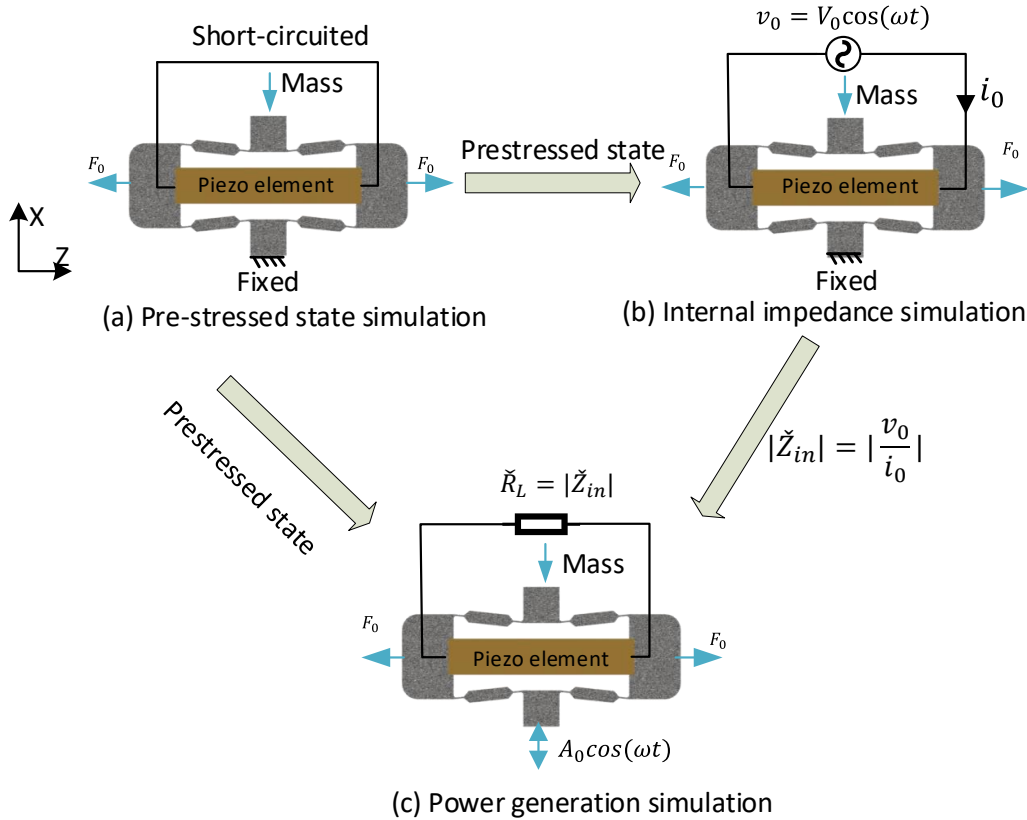
269

270   Figure 5 3D model and boundary conditions of the PSEH in (a) pre-stressed state simulation (b) internal
271   impedance simulation and (c) power generation simulation

272   The multilayer piezoelectric stack was modelled as a single-layer piezoelectric element with the same overall
273   dimensions and polarised along the z-axis to simplify the model and reduce the computational time. The number
274   of layers does not affect power output and resonance frequencies but affects some values such as impedance
275   magnitude and voltage. To facilitate the comparison between simulation and experiment, the values of the single-
276   layer stack were converted to the equivalent values of a multilayer stack by (13).

$$\Gamma = \frac{\check{\Gamma}_s}{N^2} \quad C = N^2 \check{C} \quad V_P = \frac{\check{V}_P}{N} \qquad\qquad (\,13\,)$$

277   Γ stands for the impedance magnitude $|Z_{in}|$, load resistance R_L, inductance L_m; C stands for capacitance C_P^S, C_P^T
278   and C_m; N=560 is the number of layers; V_P is the voltage output. The symbols with an accent ˘ denote the values
279   for the single-layer piezoelectric element, while those without an accent denote the converted values for multilayer
280   piezoelectric stack. The material properties used for simulation are presented in Table 1. As the multilayer
281   piezoelectric stack includes not just piezoelectric material (PIC252) but also electrodes, its elastic compliance is
282   different from the piezoelectric material. The elastic compliance along z-axis is particularly important because
283   the piezoelectric stack vibrates along this direction. The elastic compliance of the piezoelectric stack s_{33}^E was

284　estimated based on the stiffness (50 N/μm)) of the multilayer stack provided by the supplier, instead of using the
285　material properties of PIC252.

286　　　　　Table 1 the material properties of the multilayer piezoelectric stack and spring steel

Parameters	Values
Piezoelectric stack	
Density (kg/m^3)	7800
s_{11}^E ($\times 10^{-12}$ m^2/N)	16.06
s_{12}^E ($\times 10^{-12}$ m^2/N)	-5.68
s_{13}^E ($\times 10^{-12}$ m^2/N)	-7.45
s_{33}^E ($\times 10^{-12}$ m^2/N)	27.0
s_{44}^E ($\times 10^{-12}$ m^2/N)	46.99
s_{66}^E ($\times 10^{-12}$ m^2/N)	43.50
d_{31} ($\times 10^{-12}$ m/V)	-186.7
d_{33} ($\times 10^{-12}$ m/V)	399.6
d_{15} ($\times 10^{-12}$ m/V)	617.4
$\varepsilon_{11}^T/\varepsilon_0$	1852
$\varepsilon_{33}^T/\varepsilon_0$	1751
Spring steel	
Density (kg/m^3)	7850
Young's modulus (GPa)	207
Poisson's ratio	0.3

287

288　In the fabricated PSEH, the mechanical transformer was stretched to apply to static compressive stress on the
289　piezoelectric element. As a result, a static tensile force was applied to the mechanical transformer, leading to a
290　reduced inclined angle β. The reduction β is expected to reduce the stiffness and resonance frequency of the
291　PSEH, as analysed in Section 3.1. To simulate this effect, a static force F_0 was applied to the PSEH as shown in
292　Figure 5. The static force stretched the mechanical transformer and reduced β, which is the same as the case of
293　the fabricated PSEH. The static force in the FEM also introduced static tensile stress in the piezoelectric element,
294　which is opposite to the case of the fabricated PSEH. This does not affect the validity of the modelling because
295　the static stress in the piezoelectric element does not affect the power output. The magnitude of F_0 in the FEM
296　was set to a value that produced the same ΔL_z as in experiment (66 μm).

297　4.2 Boundary conditions

298　The developed FEM consists of three analysis steps incorporated in one study. Step (1), pre-stressed state
299　simulation, is a stationary analysis which computes the pre-stressed state of the PSEH as a result of the static force.
300　The pre-stressed state obtained in this step is passed to the next two steps. Step (2) and (3) are 'frequency domain,
301　perturbation analysis', which computes the response of the PSEH subjected to a harmonic perturbation fluctuating
302　around the pre-stressed state computed in Step (1). Step (2) simulates the internal impedance of the pre-stressed
303　PSEH, which is passed to Step (3) for power generation simulation. The relationship between the three steps is
304　shown in Figure 5. The boundary conditions for each step are described below. For PEHs without pre-stress, Step
305　(1) can be omitted.

306　(1) Pre-stressed state simulation

307　In this step, the piezoelectric element was short-circuited and a static force was applied to simulate the mechanical
308　responses without electromechanical coupling, as shown in Figure 5 (a). The bottom surface of the mechanical
309　transformer was fixed to make sure that enough degrees of freedom were constrained in the simulation.

310　(2) Internal impedance simulation

311　In this step, the bottom of the mechanical transformer was fixed as step (1). A harmonic voltage v_0 was applied
312　to the electrodes of the piezoelectric element, as shown in Figure 5 (b). A frequency sweep across the frequency
313　range of interest was performed. The current i_0 simulated was used to compute the internal impedance of the
314　PSEH at each frequency by

$$\check{Z}_{in} = \frac{v_0}{i_0} = |\check{Z}_{in}|e^{-j\theta_{in}} \qquad\qquad (14)$$

315 where θ_{in} is the internal impedance phase.

316 (3) Power generation simulation

317 In this step, a harmonic acceleration was applied to the bottom of the mechanical transformer as shown in Figure
318 5 (c). The electrodes of the piezoelectric element were connected to a circuit with a load resistor $\check{R}_L$. $\check{R}_L$ was set
319 to the internal impedance magnitude $|\check{Z}_{in}|$ computed in Step (2), by using the built-in operator 'withsol' provided
320 by COMSOL. In this way, during a frequency sweep, $\check{R}_L$ was always equal to $|\check{Z}_{in}|$ at the frequency that is being
321 swept. The voltage across $\check{R}_L$ was recorded to compute the electric power output. For the purpose of comparison,
322 a simulation was also performed by using the RC matching method, where $\check{R}_L$ was set to $1/\omega\check{C}_P^T$.

323 4.3 Estimation of the static force in the fabricated PSEH

324 F_0 used for internal impedance and power generation simulations is much higher than the static force in the
325 fabricated PSEH. This is because in these simulations both the mechanical transformer and the piezoelectric were
326 stretched by F_0 to produce ΔL_z=66 whereas in the fabricated PSEH only the mechanical transformer was stretched
327 to produce $\Delta L_z = 66$ µm. To estimate the static force in the fabricated PSEH, a stationary analysis was performed
328 on the mechanical transformer without the piezoelectric element, as schematically shown in Figure 6. The
329 mechanical transformer was stretched by a static force F_s along z-axis to reach a displacement of $\Delta L_z= 66$ µm.
330 This F_s was the static force applied in the fabricated PSEH.
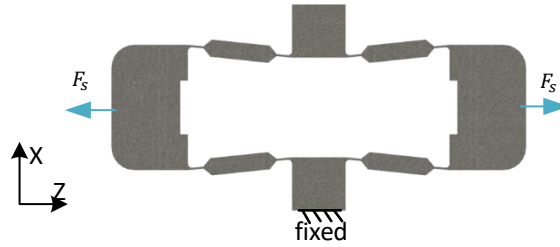
331

332 Figure 6 A schematic of the finite element model to estimate the static force F_s applied in the fabricated PSEH

333 **5. Results and discussions**

334 5.1 Experimental validation of internal impedance simulation

335 The simulated and measured internal impedance magnitudes are compared in Figure 7. In the simulation, the
336 mechanical quality factor Q_M was set to 60, which was obtained from the measured internal impedance
337 characteristics and by using (9). The static F_0 was initially set to produce ΔL_z=66 µm, which is the deformation
338 measured on the fabricated PSEH. However, with ΔL_z=66 µm the simulated resonance frequency was higher than
339 the experiment. F_0 was then adjusted until the simulated resonance frequency matched the experiment. When ΔL_z
340 =76 µm was produced, good agreement between the measured and simulated impedance was observed. Based on
341 the simulated internal impedance, the parameters of the equivalent circuit model were identified by using (3) and
342 listed in Table 2. The effective electromechanical coupling factor K was calculated by (9). Considering Q_M is
343 60, the value of $K^2 Q_M$ is 7.8, which is larger than 2. Therefore, the PSEH modelled in this work is strongly coupled.

344 Both simulated and measured internal impedance have zero-phase at 189 and 200.5 Hz. The maximum-phase is
345 observed at 195 Hz. At this frequency, impedance magnitude is 159 Ω, which is close to the value of
346 $1/(\omega_s C_P^S)$=156 Ω. This agrees with the theoretical analysis in Section 2 that the internal impedance magnitude at
347 the maximum-phase frequency is $1/(\omega_s C_P^S)$.

348   The difference in ΔL_z between simulation and experiment is attributed to (1) the geometrical difference between
349   the designed and fabricated mechanical transformer due to manufacturing tolerance; (2) the properties of the
350   piezoelectric material typically varies ±5-10% compared to the datasheet.
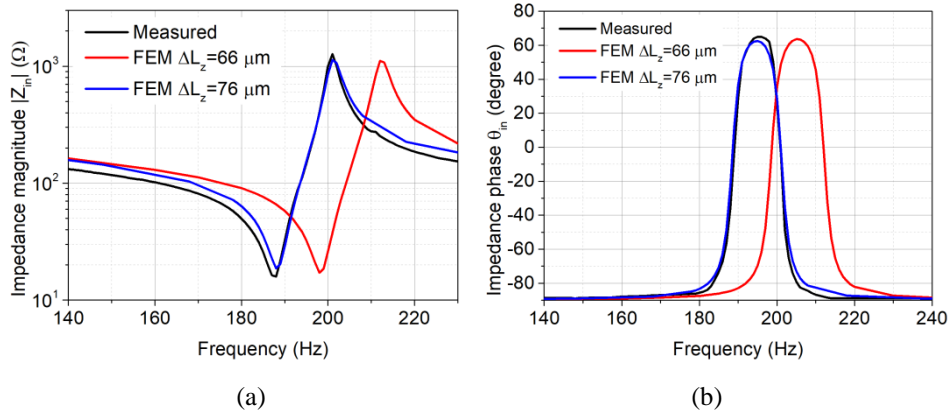
351
352   (a)   (b)
353   Figure 7 Comparison of measured and simulated internal impedance of the PSEH (a) impedance magnitude and
354   (b) impedance phase

355   Table 2 Lumped parameters identified from the simulated internal impedance of the PSEH

Parameters	Values	Unit
C_P^S	5.40	μF
C_m	0.71	μF
C_P^T	6.11	μF
ω_s	1190 (189)	Rad/s (Hz)
L_m	1.00	H
R_m	19.93	Ω
K	0.36	-

356

357   5.2 Estimation of the static force in the fabricated PSEH

358   When ΔL_z=76 µm was produced in the FEM (Figure 8 (a)), the static force F_0 was 4100 N. The corresponding
359   ΔL_x was found to be 770 µm, as shown in Figure 8 (b). The displacement ratio of the PSEH, $\Delta L_x/\Delta L_z$ in the FEM
360   is 10.13, which is close to the value of 9.50 in the experiment. Without the piezoelectric element, F_s=360 N was
361   required to produce ΔL_z = 76 µm as shown in Figure 9 (a). Therefore, the static force applied in the fabricated
362   PSEH is estimated to be 360 N. With F_s=360 N, ΔL_x of the mechanical transformer alone is 807 µm (Figure 9
363   (b)), which is slightly higher than that of the simulated PSEH. The slight difference in ΔL_x reflects the influence
364   of the piezoelectric element on the amplification effect of the mechanical transformer.
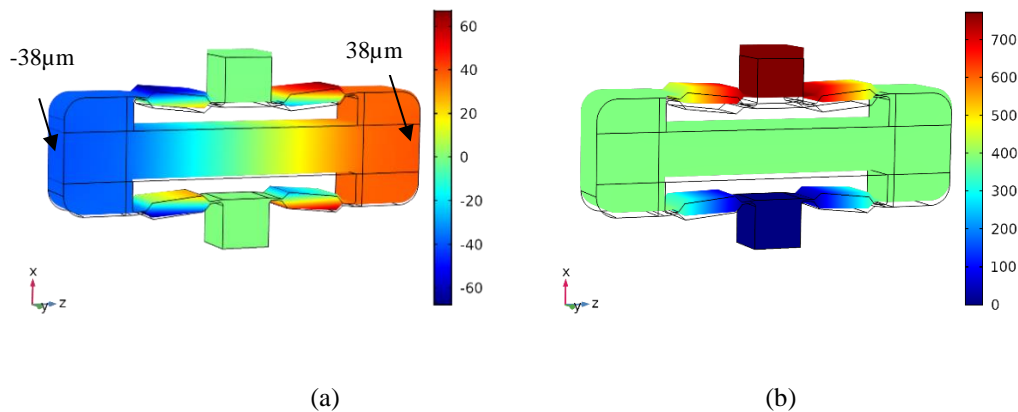
365
366
367   (a)   (b)
368   Figure 8 Displacement of the PSEH due to the static force F_0=4100 N (a) z-axis displacement and (b) x-axis
369   displacement. Unit of the colour legend: µm
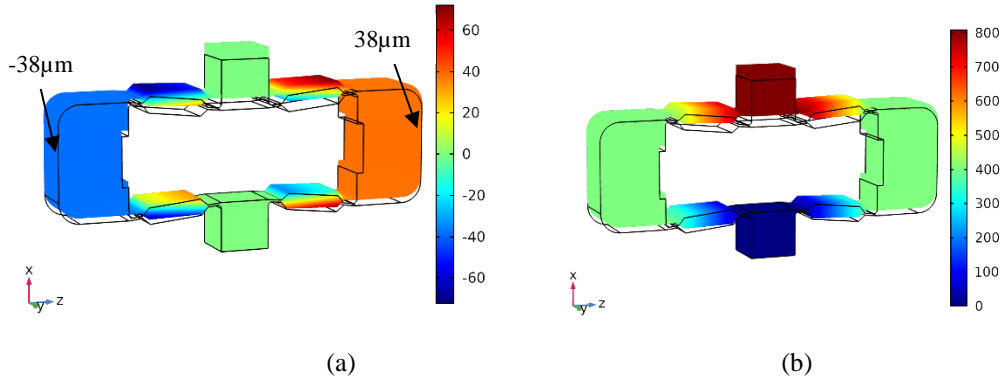
370
371 (a)   (b)
372 Figure 9 Displacement of the mechanical transformer due to F_s=360 N: (a) z-axis displacement and (b) x-axis
373   displacement. Unit of the colour legend: µm

374 5.3 Experimental validation of power generation simulation

375 The measured and simulated electric power outputs of the PSEH actuated at 2.5 m/s^2 are compared in Figure 10
376 (a). The corresponding load resistance used for the power generation is presented in Figure 10 (b). When the
377 internal impedance magnitude $|Z_{in}|$ is used as the load resistance, the simulated electric power shows two nearly
378 identical peaks of 5.19 and 5.22 mW at 189 and 200.5 Hz, respectively. Both frequencies are the zero-phase
379 frequency, as identified in Section 5.1. The impedance magnitudes at these two frequencies are 19.9 and 1130.2
380 Ω, respectively. Moreover, the simulated power shows a local minimum of 4.21 mW at 195 Hz, which is the
381 maximum-phase frequency. Simulations were performed at each frequency with various load resistance to confirm
382 that the power output with $R_L = |Z_{in}|$ is the maximum at each frequency and the impedance magnitudes are the
383 optimal load resistance. Representative results are presented in Figure 11. When actuated at 189 Hz, the PSEH
384 produces the maximum power of 5.19 mW at 19.5 Ω.
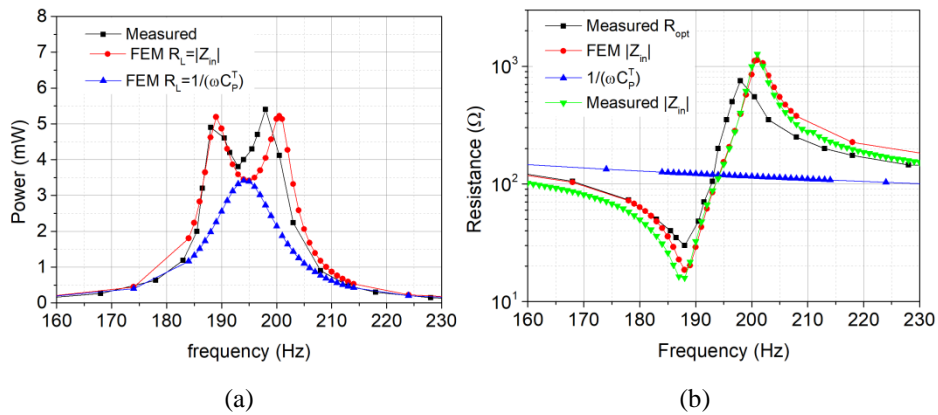
385
386 (a)   (b)
387 Figure 10 Comparison of the measured and simulated performance of the PSEH actuated at 2.5 m/s^2 (a) electric
388   power output (b) load resistance and internal impedance magnitude

389 In the experiment, the power output (Figure 10 (a)) shows two peaks of 4.90 mW and 5.4 mW at 188 and 198 Hz,
390 respectively. A local minimum of 3.8 mW was recorded at 193 Hz. The optimal resistance at each frequency was
391 measured by varying the connected load resistance until the maximum power output was recorded. Typical results
392 are shown in Figure 11. The PSEH at 188 Hz produced 4.90 mW with R_L=35 Ω. The experiment results in Figure
393 10 show good agreement with the simulation although slight discrepancy is observed. Moreover, the measured
394 power peaks are located at 188 and 198 Hz, instead of the zero-phase frequencies (189 and 200.5 Hz) identified
395 in the measured internal impedance. This is caused by the nonlinear behaviours of piezoelectric material in the
396 experiment, which was not modelled in the simulation. When piezoelectric materials are actuated to operate at
397 high stress/strain level, the material properties will change and the behaviours become nonlinear, leading to
398 phenomena such as reduced resonance frequency and increased mechanical loss [19, 37]. These nonlinear
399 behaviours also caused the difference between the measured optimal resistance R_{opt} and the measured impedance

magnitude since the impedance was measured at a low voltage level (0.5 V peak to peak) with little nonlinear
behaviour.
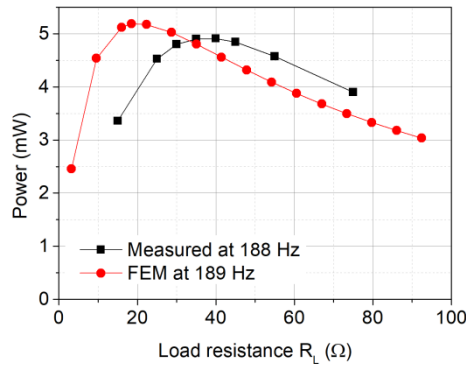
403 Figure 11 Electric power outputs against load resistance at the first power-peak frequency

When the RC matching method is used, i.e. $R_L = 1/(\omega C_P^T)$, the simulated power shows only one peak of 3.42 mW at 195 Hz, in contrast to two power peaks of 5.2 mW when $R_L = |Z_{in}|$. Both simulation configurations produce the same power output at the maximum-phase frequency (195 Hz). This is because the value of $1/(\omega C_P^T)$ at 195 Hz is 134 Ω, which is close to the impedance magnitude $1/(\omega_s C_P^T)$ at this frequency. This can be verified by the intersection of $|Z_{in}|$ and $R_L = 1/(\omega C_P^T)$ at around 195 Hz, as shown in Figure 10 (b). Moreover, at frequencies outside the resonance (>205 Hz and <175 Hz), the same power outputs are observed with the two simulation configurations due to the relatively small difference between $|Z_{in}|$ and $1/(\omega C_P^T)$. At other frequencies, the simulation with $R_L = 1/(\omega C_P^T)$ underestimates the power output.

Therefore, with the $|Z_{in}|$ as the optimal load resistance, the FEM can accurately predict the power output of the PSEH in both resonance and off-resonance regions, whereas the FEM with RC matching can only predict the power output at the maximum-phase frequency and at off-resonance.

5.4 Effects of $K^2 Q_M$

The theoretical analysis in Section 2 indicates that the coupling efficiency figure of merit $K^2 Q_M$ determines if there exist two power peaks of a PEH. When $K^2 Q_M > 2$, the PEH is strongly coupled and has two power peaks; when $K^2 Q_M \leq 2$, the PEH is weakly coupled and has a single power peak. To verify the ability of the FEM to predict such characteristics, simulations were performed on the PSEH with $K^2 Q_M$ of 7.8, 3.9, 2 and 1.3. This was achieved by keeping the effective electromechanical factor K constant at 0.36 while changing the mechanical quality factor Q_M to be 60, 30, 15 and 10, respectively. The simulated electric power outputs of the PSEH actuated at 2.5 m/s² along with the impedance-phase are presented in Figure 12.

423

424
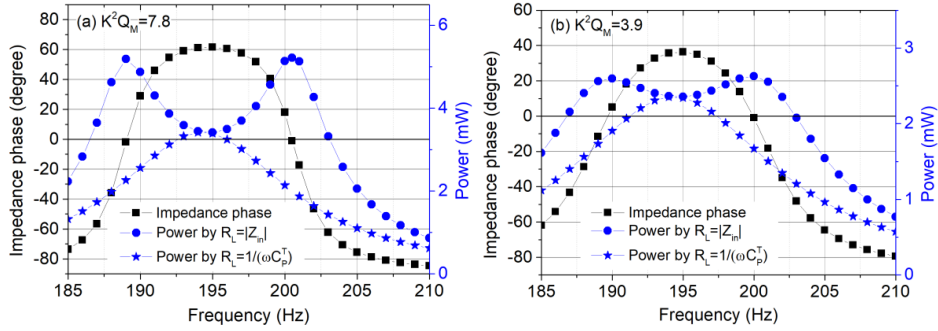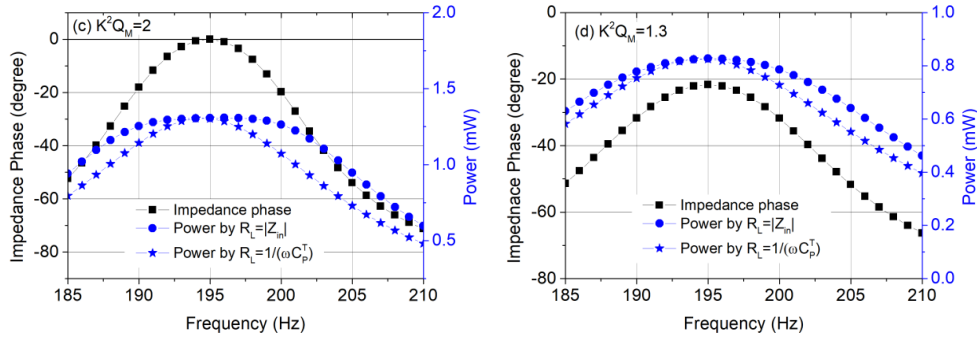
Figure 12 Simulated electric power output and impedance-phase of the PSEH with different values of K^2Q_M (a) $K^2Q_M = 7.8$, (b) $K^2Q_M = 3.9$, (c) $K^2Q_M = 2$, and (d) $K^2Q_M = 1.3$

When $K^2Q_M = 7.8$ and $R_L = |Z_{in}|$, the power peaks appear at $f_{01} = 189$ Hz and $f_{02} = 200.5$ Hz. The local minimum power is located at the maximum-phase frequency ($f_m = 195$ Hz). The frequency range between f_{10} and f_{02} is 11.5 Hz. With $R_L = 1/\omega C_P^T$, the single peak power is located at $f_m = 195$ Hz. When the K^2Q_M is reduced to 3.9 (Figure 12 (b)), the PSEH has similar power-frequency characteristics as $K^2Q_M = 7.8$ but with power peaks reduced from 5.22 mW to 2.62 mW and the frequency range between f_{01} and f_{02} decreased from 11.5 Hz to 10 Hz. The reduction in the power output is due to the increased mechanical damping by decreasing Q_M. Because of the decrease in Q_M, the value of R_m is increased according to Eq. (9). This leads to a decrease in the diameter of the G-B circle, as shown in Figure 13. As a result, the frequency range between f_{01} and f_{02} is decreased. When K^2Q_M is 2, the G-B cicle is tangent to $B=0$. As a result, f_{01}, f_{02} and f_m merges to one frequency—195 Hz and the PSEH has a single power peak at this frequency (Figure 12 (c)). As the value of K^2Q_M is further decreased, the PSEH has no zero--phases and a sinlge power peak is observed at the maximum-phase-frequency. The performance of the PSEH simulated by the FEM, therefore, agrees well with the theoretical prediction in Section 2.2.

It can be also noted from Figure 12 that as K^2Q_M is reduced, the descrepancy of power output between $R_L = |Z_{in}|$ and RC matching is decreased. This suggests that when K^2Q_M is low enough, the RC matching can be a valid approximation for the PSEH at the resonance region.


442
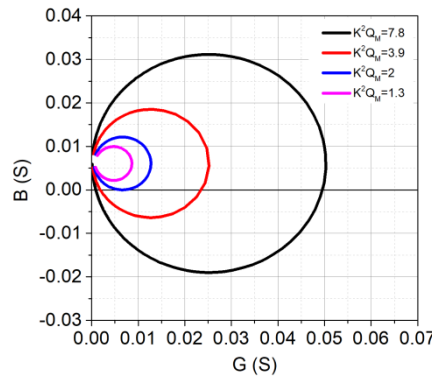
443

Figure 13 G-B locus of the PSEH with different values of K^2Q_M

444   5.5 Effects of static force

445   The simulated effects of the F_0 on the power output of the PSEH is presented in Figure 14. As F_0 increases, the
446   resonance frequency decreases and the peak power increases. This is because as F_0 increases, the angle β of the
447   mechanical transformer is reduced, which can be verified by the increase of $\Delta L_x/\Delta L_z$ with F_0 in Table 3 . As a
448   result, the stiffness of the mechanical transformer is decreased, leading to the decrease of the resonance frequency.
449   Moreover, the reduction of β results in an increased force amplification effect as suggested by (11), giving rise
450   to the increase in the power generation.
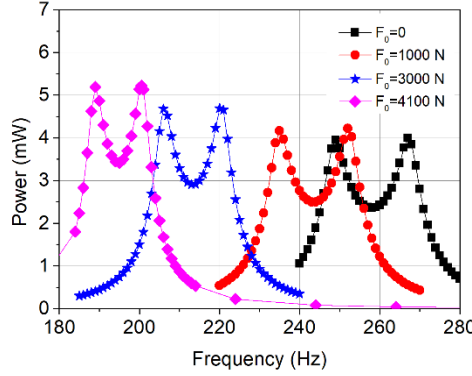
451

452   Figure 14 Effects of the static force F_0 on the power output and resonance frequency shift of the PSEH

453   Table 3 the static displacement ΔL_z, ΔL_x, displacement ratio $\Delta L_z/\Delta L_z$ and static force F_s corresponding to each
454   value of F_0

F_0 (N)	ΔL_z (µm)	ΔL_x (µm)	$\Delta L_x/\Delta L_z$	F_s (N)
1000	19	175	9.2	60
3000	57	554	9.8	230
4100	76	770	10.1	360

455 ## 6. Conclusions

456   In this work, a finite element model (FEM) for strongly-coupled and pre-stressed piezoelectric energy harvester
457   (PEH) was developed and experimentally validated. The FEM enables the efficient and accurate prediction of the
458   electric power output of both weakly and strongly coupled PEHs. The model was developed for a piezoelectric
459   stack energy harvester (PSEH) with a force amplifier, but the method can be applied to any linear PEHs or
460   nonlinear PEHs that can be linearized around the operating point.

461   The equivalent circuit model (ECM) of PEHs was first derived from an analytical model. Based on the ECM, the
462   internal impedance network of PEHs was identified. According to the maximum power transfer theorem, the load
463   resistance should be matched to the internal impedance magnitude of PEHs to obtain the maximum power
464   generation although the theoretical maximum power transfer only occurs when the impedance-phase is zero.
465   Analysis of the conductance and susceptance locus of the internal admittance suggested that the availability of
466   zero-phase frequency depended on the value of $K^2 Q_M$, with K being the electromechanical coupling factor and
467   Q_M being the mechanical quality factor.

468   Since the internal impedance magnitude should be used as the optimal load resistance, the proposed finite element
469   modelling method first analysed the internal impedance of the PEH, the magnitude of which was then used as the
470   load resistance for power output simulation. The modelling method was applied to a pre-stressed piezoelectric
471   stack energy harvester (PSEH) with a mechanical transformer. Comparisons between simulation and experiment
472   showed that the developed FEM was able to precisely predict both the internal impedance and electric power
473   output of the strongly coupled PSEH at any frequencies. The simulated power output characteristics of the PSEH
474   at different values of $K^2 Q_M$ also agreed well with the theoretical prediction. When the impedance of the internal
475   capacitor of the PSEH was used as the optimal load resistance (RC matching), the FEM was valid at off-resonance

476 and the maximum-phase frequency regardless of the degree of the electromechanical coupling. At resonance, the
477 FEM with RC matching underestimated the power output for the strongly-coupled PSEH, although the error
478 decreases with the value of $K^2 Q_M$.

Acknowledgement

References

483 [1] A. Toprak and O. Tigli, "Piezoelectric energy harvesting: State-of-the-art and challenges," (in
484   English), *Applied Physics Reviews,* Review vol. 1, no. 3, Sep 2014, Art no. 031104, doi:
485   10.1063/1.4896166.
486 [2] Y. Kuang, T. Ruan, Z. J. Chew, and M. Zhu, "Energy harvesting during human walking to
487   power a wireless sensor node," *Sensors and Actuators A: Physical,* vol. 254, pp. 69-77, 2/1/
488   2017, doi: http://dx.doi.org/10.1016/j.sna.2016.11.035.
489 [3] H. Li, C. Tian, and Z. D. Deng, "Energy harvesting from low frequency applications using
490   piezoelectric materials," *Applied Physics Reviews,* vol. 1, no. 4, p. 041301, 2014.
491 [4] S. Priya, "Advances in energy harvesting using low profile piezoelectric transducers," (in
492   English), *Journal of Electroceramics,* Article vol. 19, no. 1, pp. 167-184, Sep 2007, doi:
493   10.1007/s10832-007-9043-4.
494 [5] N. G. Elvin, A. A. Elvin, and M. Spector, "A self-powered mechanical strain energy sensor,"
495   *Smart Materials and structures,* vol. 10, no. 2, p. 293, 2001.
496 [6] T.-B. Xu *et al.*, "Energy harvesting using a PZT ceramic multilayer stack," *Smart Materials
497   and Structures,* vol. 22, no. 6, p. 065015, 2013.
498 [7] A. Erturk and D. J. Inman, "An experimentally validated bimorph cantilever model for
499   piezoelectric energy harvesting from base excitations," *Smart materials and structures,* vol. 18,
500   no. 2, p. 025009, 2009.
501 [8] Y. Shu and I. Lien, "Analysis of power output for piezoelectric energy harvesting systems,"
502   *Smart materials and structures,* vol. 15, no. 6, p. 1499, 2006.
503 [9] Y. Liao and H. A. Sodano, "Structural effects and energy conversion efficiency of power
504   harvesting," *Journal of Intelligent Material Systems and Structures,* vol. 20, no. 5, pp. 505-514,
505   2009.
506 [10] W. Wang, J. Cao, C. R. Bowen, S. Zhou, and J. Lin, "Optimum resistance analysis and
507   experimental verification of nonlinear piezoelectric energy harvesting from human motions,"
508   *Energy,* vol. 118, pp. 221-230, 2017.
509 [11] J. M. Renno, M. F. Daqaq, and D. J. Inman, "On the optimal energy harvesting from a vibration
510   source," *Journal of sound and vibration,* vol. 320, no. 1-2, pp. 386-405, 2009.
511 [12] F. Goldschmidtboeing, M. Wischke, C. Eichhorn, and P. Woias, "Parameter identification for
512   resonant piezoelectric energy harvesters in the low-and high-coupling regimes," *Journal of
513   Micromechanics and Microengineering,* vol. 21, no. 4, p. 045006, 2011.
514 [13] Y. Liao and H. A. Sodano, "Model of a single mode energy harvester and properties for optimal
515   power generation," *Smart Materials and Structures,* vol. 17, no. 6, p. 065026, 2008.
516 [14] N. G. Elvin and A. A. Elvin, "A coupled finite element—circuit simulation model for analyzing
517   piezoelectric energy generators," *Journal of Intelligent Material Systems and Structures,* vol.
518   20, no. 5, pp. 587-595, 2009.
519 [15] H. Abdelmoula, N. Sharpes, A. Abdelkefi, H. Lee, and S. Priya, "Low-frequency Zigzag energy
520   harvesters operating in torsion-dominant mode," *Applied Energy,* vol. 204, pp. 413-419, 2017.
521 [16] N. G. Elvin and A. A. Elvin, "A general equivalent circuit model for piezoelectric generators,"
522   *Journal of Intelligent Material Systems and Structures,* vol. 20, no. 1, pp. 3-9, 2009.
523 [17] Y. Yang and L. Tang, "Equivalent circuit modeling of piezoelectric energy harvesters," *Journal
524   of intelligent material systems and structures,* vol. 20, no. 18, pp. 2223-2235, 2009.

[18] N. Kong, D. S. Ha, A. Erturk, and D. J. Inman, "Resistive Impedance Matching Circuit for Piezoelectric Energy Harvesting," (in English), *Journal of Intelligent Material Systems and Structures,* Article; Proceedings Paper vol. 21, no. 13, pp. 1293-1302, Sep 2010, doi: 10.1177/1045389x09357971.

[19] A. Lei, R. Xu, L. M. Borregaard, M. Guizzetti, O. Hansen, and E. V. Thomsen, "Impedance based characterization of a high-coupled screen printed PZT thick film unimorph energy harvester," *Journal of Microelectromechanical Systems,* vol. 23, no. 4, pp. 842-854, 2014.

[20] Y. Qi, N. T. Jafferis, K. Lyons, C. M. Lee, H. Ahmad, and M. C. McAlpine, "Piezoelectric Ribbons Printed onto Rubber for Flexible Energy Conversion," (in English), *Nano Letters,* Article vol. 10, no. 2, pp. 524-528, Feb 2010, doi: 10.1021/nl903377u.

[21] J. Liang and W.-H. Liao, "Impedance modeling and analysis for piezoelectric energy harvesting systems," *IEEE/ASME Transactions on Mechatronics,* vol. 17, no. 6, pp. 1145-1157, 2012.

[22] C. Cheng, Z. Chen, H. Shi, Z. Liu, and Y. Xiong, "System-Level Coupled Modeling of Piezoelectric Vibration Energy Harvesting Systems by Joint Finite Element and Circuit Analysis," *Shock and Vibration,* vol. 2016, 2016.

[23] D. Pan and F. Dai, "Design and analysis of a broadband vibratory energy harvester using bi-stable piezoelectric composite laminate," *Energy conversion and management,* vol. 169, pp. 149-160, 2018.

[24] D. Wang, J. Mo, X. Wang, H. Ouyang, and Z. Zhou, "Experimental and numerical investigations of the piezoelectric energy harvesting via friction-induced vibration," *Energy conversion and management,* vol. 171, pp. 1134-1149, 2018.

[25] M. Zhu, E. Worthington, and J. Njuguna, "Analyses of power output of piezoelectric energy-harvesting devices directly connected to a load resistor using a coupled piezoelectric-circuit finite element method," *Ultrasonics, Ferroelectrics and Frequency Control, IEEE Transactions on,* vol. 56, no. 7, pp. 1309-1317, 2009.

[26] X. Li, D. Upadrashta, K. Yu, and Y. Yang, "Sandwich piezoelectric energy harvester: Analytical modeling and experimental validation," *Energy conversion and management,* vol. 176, pp. 69-85, 2018.

[27] K. Yang, D. Alice, and Z. Meiling, "A sandwiched piezoelectric transducer with flex end-caps for energy harvesting in large force environments," *Journal of Physics D: Applied Physics,* vol. 50, no. 34, p. 345501, 2017. [Online]. Available: http://stacks.iop.org/0022-3727/50/i=34/a=345501.

[28] Y. Kuang and M. Zhu, "Design study of a mechanically plucked piezoelectric energy harvester using validated finite element modelling," *Sensors and Actuators A: Physical,* vol. 263, pp. 510-520, 2017/08/15/ 2017, doi: http://dx.doi.org/10.1016/j.sna.2017.07.009.

[29] A. Ramos-Fernandez, J. Gallego-Juarez, and F. Montoya-Vitini, "Automatic system for dynamic control of resonance in high power and high Q ultrasonic transducers," *Ultrasonics,* vol. 23, no. 4, pp. 151-156, 1985.

[30] Y. Kuang, Y. Jin, S. Cochran, and Z. Huang, "Resonance tracking and vibration stablilization for high power ultrasonic transducers," *Ultrasonics,* vol. 54, no. 1, pp. 187-194, 2014.

[31] F. Qian, T.-B. Xu, and L. Zuo, "Design, optimization, modeling and testing of a piezoelectric footwear energy harvester," *Energy conversion and management,* vol. 171, pp. 1352-1364, 2018.

[32] X. Wang, Z. Shi, J. Wang, and H. Xiang, "A stack-based flex-compressive piezoelectric energy harvesting cell for large quasi-static loads," *Smart Materials and Structures,* vol. 25, no. 5, p. 055005, 2016.

[33] W. Chen, Y. Wang, and W. Deng, "Deformable force amplification frame promoting piezoelectric stack energy harvesting: Parametric model, experiments and energy analysis," *Journal of Intelligent Material Systems and Structures,* vol. 28, no. 7, pp. 827-836, 2017.

[34] M. Evans, L. Tang, and K. C. Aw, "Modelling and optimisation of a force amplification energy harvester," *Journal of Intelligent Material Systems and Structures,* p. 1045389X18754352, 2018.

[35] J. Cho, R. Richards, D. Bahr, C. Richards, and M. Anderson, "Efficiency of energy conversion by piezoelectrics," *Applied physics letters,* vol. 89, no. 10, pp. 104107-104107-3, 2006.

579   [36]   L. Wang, S. Chen, W. Zhou, T.-B. Xu, and L. Zuo, "Piezoelectric vibration energy harvester
580   with two-stage force amplification," *Journal of Intelligent Material Systems and Structures,* vol.
581   28, no. 9, pp. 1175-1187, 2017.
582   [37]   Y. Kuang, M. Sadiq, S. Cochran, and Z. Huang, "High-power characterization of a microcutter
583   actuated by PMN-PT piezocrystals," *IEEE transactions on ultrasonics, ferroelectrics, and*
584   *frequency control,* vol. 62, no. 11, pp. 1957-1967, 2015.

585